Materials Advances

ROYAL SOCIETY OF CHEMISTRY

PAPER

View Article Online
View Journal | View Issue

Cite this: *Mater. Adv.*, 2026, 7, 5290

Tuning magnetic order and spin–exciton interactions in $MnPSe_3$ *via* Cu substitution

Mohamed Nawwar,[a] Alexander Blackston,[a] Sogol Lotfi,[a] Ziling Deng,[a] Alexander Reifsnyder,[a] David McComb,[a] Wolfgang Windl,[ab] Vicky Doan-Nguyen Trigg[a] and Roberto C. Myers*[abc]

Received 20th March 2026,
Accepted 22nd April 2026

DOI: 10.1039/d6ma00397d

rsc.li/materials-advances

We report a comprehensive investigation of Cu-substituted $MnPSe_3$ [$Mn_{1-x}Cu_{2x}PSe_3$ (x = 0–0.2)], a layered van der Waals magnetic semiconductor, revealing a unique interplay between chemical substitution, magnetism, and excitonic behavior. Structural analyses demonstrate that Cu(I) ions substitute Mn(II) at distinct crystallographic sites, producing anisotropic lattice expansion. With increasing Cu content, magnetic susceptibility measurements show a systematic suppression of antiferromagnetic order and a transition to a paramagnetic state beyond $x \geq 0.15$. Concurrently, thermal conductivity decreases due to enhanced phonon scattering. Photoluminescence spectroscopy uncovers three sub-bandgap excitons, two of which show pronounced redshifts as a function of temperature, indicating strong spin–exciton coupling. This work establishes chemical substitution as a powerful tool to tune magnetism and spin–exciton interactions in 2D materials, opening new design strategies for spintronic and quantum optoelectronic platforms.

1 Introduction

Two-dimensional (2D) van der Waals (vdW) magnetic materials offer a rich platform for controlling spin interactions, topological properties, and collective excitations in layered systems. Their atomic thinness and intrinsic anisotropy enable magnetic properties to be tuned *via* electrostatic gating, strain, doping, and heterostructuring—making them compelling candidates for next-generation spintronic and magnonic devices. In recent years, intrinsic magnetism has been discovered in vdW compounds such as $MnPSe_3$, $MnPS_3$, $FePS_3$, CrI_3, $CrCl_3$, $Cr_2Ge_2Te_6$, VSe_2, and $MnSe_2$.[1–8] In many of these systems, magnetic order and Berry curvature can be modulated by strain, electric, and magnetic fields.[9–14] The MPX_3 (M = Cr, Mn, Fe, Co, Ni, Zn, Cd; X = S, Se) family of materials has shown great potential thanks to the many discoveries and predictions of topological magnons, magnon–phonon hybridization, excitonic insulators and magneto-electric coupling.[13,15–19]

Elemental doping has shown great potential in tuning various physical properties in different families of materials.[20–23] Among various approaches to tune magnetism in vdW magnets, atomic substitution has emerged as a powerful route to systematically perturb exchange interactions and spin–lattice coupling. The MPX_3 family consists of layered materials that crystallize in monoclinic ($C2/m$) or trigonal ($R\bar{3}$) structures with transition metal cations forming honeycomb sublattices.[24,25] Substitution of magnetic ions with other magnetic species has been widely explored in compounds such as $Mn_xFe_{1-x}PS_3$, $Mn_xNi_{1-x}PS_3$, $Mn_{1-x}Fe_xPSe_3$, $Ni_{1-x}Fe_xPS_3$, and $Fe_{0.5}Ni_{0.5}PS_3$, leading to modified anisotropies, ordering temperatures, and magnetic structures.[26–34] In contrast, the effects of substituting magnetic ions with non-magnetic species remain comparatively unexplored. Such substitutions offer a route to investigate dilute or frustrated magnetic orderings, and may shed light on how non-magnetic impurities influence spin coherence, transport, and exciton–spin interactions in layered magnets.

$MnPSe_3$, a member of the MPX_3 family, crystallizes in the trigonal $R\bar{3}$ structure, with Mn(II) ions forming an antiferromagnetic honeycomb lattice in the ab plane (Fig. 1a and b).[35] Prior work has shown that monovalent Cu(I) can coexist with divalent Mn(II) in $MnPS_3$ forming $Mn_{0.87}Cu_{0.26}PS_3$.[36,37] In the selenide family, Cu_2PSe_3 is known to exist in both monoclinic ($P2_1/c$) and triclinic ($P\bar{1}$) structures.[38] These findings suggest that Cu(I) may be incorporated into $MnPSe_3$ as a structural and electronic dopant, potentially modulating magnetic order while preserving crystallinity.

In this work, we demonstrate successful Cu substitution in $MnPSe_3$ across the solid solution $Mn_{1-x}Cu_{2x}PSe_3$ (x = 0–0.2), and investigate its effects on structure, magnetism, and excitonic optical response. Cu(I) is found to lie in trigonal coordination with Se, leading to anisotropic lattice expansion and progressive suppression of antiferromagnetic order. At substitution levels

[a] *Department of Materials Science and Engineering, The Ohio State University, Columbus, OH 43210, USA. E-mail: myers.1079@osu.edu*
[b] *Department of Physics, The Ohio State University, Columbus, OH 43210, USA*
[c] *Department of Electrical and Computer Engineering, The Ohio State University, Columbus, OH 43210, USA*

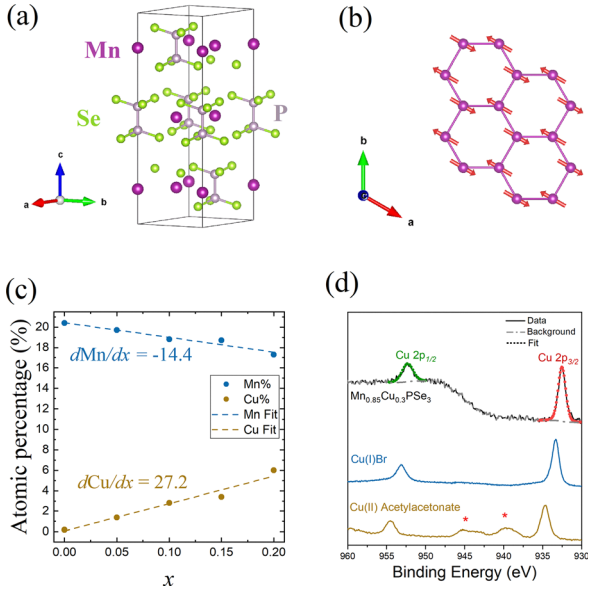

Fig. 1 (a) Crystal structure of $MnPSe_3$. (b) The honeycomb structure of Mn(II) in the *ab* plane shows the antiferromagnetic order of the spins along the *ab* plane. (c) The change in the atomic percentage for both Mn and Cu as a function of the nominal value *x*. The rate of change of Cu is twice that of Mn, indicating that the stoichiometry of the solid solution is $Mn_{1-x}Cu_{2x}PSe_3$. (d) The XPS spectrum for the $x = 0.15$ sample and the standards, Cu(I)Br and Cu(II) acetylacetonate. The spectrum for the studied Cu-substituted compound matches well with the Cu(I)Br standard and does not show any of the prominent Cu(II) satellite (red asterisks) signatures, confirming monovalency of the substituted copper ions.

$x \geq 0.15$, the material becomes paramagnetic down to 2 K. Photoluminescence spectra for $x = 0$, 0.05, and 0.2 reveal three sub-bandgap excitonic features, two of which redshift with temperature—an effect that is most pronounced in compositions with stronger antiferromagnetic order. These results suggest that excitons in $MnPSe_3$ couple to the spin lattice and that Cu substitution weakens this coupling by disrupting magnetic correlations. Together, our findings highlight the use of non-magnetic atomic substitution as a versatile tool to tune magnetic order and spin–exciton interactions in 2D vdW materials.

2 Experimental

2.1 Synthesis and crystal growth

Polycrystalline powder samples of the solid solution $Mn_{1-x}Cu_{2x}PSe_3$ ($x = 0$, 0.05, 0.1, 0.15, 0.2 and 0.25) were synthesized using conventional solid-state synthesis technique in an inert environment. Stoichiometric amounts of Mn (Sigma Aldrich 99.9%), Cu (Sigma Aldrich 99.5%), P (Sigma Aldrich, red, 99.99%), and Se (Sigma Aldrich, 99.5%) were ground using an agate mortar and pestle inside an Ar-filled glove box (<5 ppm H_2O, O_2). Chemicals were used without purification with a mass loading of 1.5 g. Powder elemental precursors were loaded into a 7 mm inner diameter fused silica tube and sealed under vacuum (<1 torr). The samples were then placed in a box furnace at 600 °C for 6 days with a ramp rate of 5 °C min^{-1} and a cooling rate of 10 °C min^{-1}. Products were then ground using an agate mortar and pestle and stored under ambient conditions. No degradation or oxidation was observed over time.

Single crystals of the alloys used for the thermal conudctivity and optical studies were grown using Chemical Vapor Transport (CVT) method. Resulting polycrystalline powdered samples were mixed with 0.03 g of iodine (transport gas) and then loaded into a fused silica tube and sealed under vacuum (<1 Torr). During the sealing, the precursors were immersed in liquid nitrogen to prevent the evaporation of iodine. The sample was then placed in a two-zone furnace with T_{hot} at 650 °C and T_{cold} at 600 °C for one week with a ramp rate of 5 °C min^{-1} and cooling rate of 0.1 °C min^{-1}.

2.2. Synchrotron X-ray diffraction (XRD) and pair distribution functions (PDF)

XRD and PDF data were obtained at Argonne National Lab's Advanced Photon Source, beamline 17-BM-B, with $\lambda = 0.24012$ Å at sample-to-detector distances of 700 mm and 200 mm, respectively. Data processing and Rietveld refinement were conducted using PDFgetX3[39] and GSAS-II.[40]

2.3. X-ray photoelectron spectroscopy (XPS)

XPS measurement was conducted using a Kratos Axis Ultra XPS instrument with a monochromatic Al X-ray source. XPS spectra were fit by Voigt functions with Shirley baselines using CasaXPS.[41] Adventitious C 1s was used for calibration at 284.5 eV.

2.4. Magnetic susceptibility

Magnetic susceptibility measurements were done using a Quantum Design MPMS3 SQUID with a 7T magnet. Both field-cooled (FC) and zero field-cooled (ZFC) measurements were done under an applied magnetic field of 1T.

2.5. Thermal conductivity

Samples were mounted at the edge of a copper block that acts as a heat sink. A 120 Ω resistor was mounted at the opposite side of the sample and used as a heater to send a heat flux across the sample. Two type T thermocouples were placed on one side of the sample to measure the temperature difference. All parts were adhered using silver epoxy. The samples were then placed in a vacuumed environment inside a Lakeshore cryostat. The voltages across the thermocouples were read using a 2182A Keithley nanovoltmeter. The cryostat temperature was controlled *via* a 331 Lakeshore temperature controller. The temperature was allowed to stabilize for 20 minutes before the sample heater was turned on. The temperature gradient was allowed to stabilize for 5 minutes before measuring.

2.6. Photoluminescence spectroscopy

Spectrally resolved photoluminescence measurements were taken in the reflection geometry using a tunable Ti-sapphire laser (Coherent Chameleon Ultra II) in conjunction with a SHG and THG generation system (Coherent Vue) as the excitation source. Focus was obtained using a 150 mm focal length achromatic lens. An excitation wavelength of 250 nm (4.96 eV) was used with a power of 1 mW leading to a power density of

0.13 W cm^{-2}. PL measurements were conducted on different sample locations and no degradation in PL spectra were detected even after long (>1 h) laser exposure periods mirroring previous studies that found no laser degradation in $MnPSe_3$ at similar power densities.[16]The reflected beam and photoluminescence was sent through a 265 nm long pass filter to filter out elastically scattered light and then analyzed using a 1200 g mm^{-1}, 500 nm blaze reflective diffraction grating and Teledyne Vision Solutions Pixis 400 CCD camera housed inside of a Princeton Instruments Acton Series SP-2500i spectrometer. All photoluminescence measurements were carried out in a closed-loop helium cryostat (Montana Instruments Cryostation S50) that could be cooled to 8 K.

2.7. Absorption measurement

The beam from a halogen lamp (Ocean Optics DH-2000) is collimated and then focused through the flakes, which were less than 2 mm wide and exfoliated onto glass slides, with a 40× reflective objective. A second 40× reflective objective was used to re-collimate the transmitted light. A diffraction grating spectrometer then spectrally resolves the light intensity. The transmitted spectrum is then spectrally analyzed using a 1200 g mm^{-1}, 500 nm blaze reflective diffraction grating and Teledyne Vision Solutions Pixis 400 CCD camera housed inside of a Princeton Instruments Acton Series SP-2150i spectrometer. Transmission along the beam path is measured without the flake in the beam path to collect a reference spectrum. All measurements were completed at room temperature.

3 Results and discussion

3.1. Structural characterization

3.1.1. Stoichiometry. Inductively Coupled Plasma (ICP) measurement was conducted to determine the stoichiometry of the sample. During acid digestion, some selenium was lost. Therefore, the weight and atomic percentages calculated are not accurate. Alternatively, we calculated the rate of change of Mn and Cu for samples with nominal values up to x = 0.2. The change for both Mn and Cu was found to be linear, where the rate of change for Cu is twice that for Mn, indicating that the stoichiometry is $Mn_{1-x}Cu_{2x}PSe_3$ (Fig. 1(c)).

The XPS spectrum for x = 0.15 depicts Cu $2p_{3/2}$ peak with FWHM of 1.13, centered at 932.52 eV and separated from Cu $2p_{1/2}$ (FWHM of 1.56) by 19.80 eV (Fig. 1(d)), consistent with previous reports for Cu_2O.[42] Cu(II)acetylacetonate and Cu(I)Br were used as standards for comparison. The shift in the peak center of Cu $2p_{3/2}$ and the absence of the shake-up peaks around 940 eV and 945 eV (marked with red asterisks in Fig. 1(d)) confirm that Cu exists as monovalent. In addition, the Cu LMM auger peak for this sample appears at 569.90 eV binding energy, which is 916.70 eV kinetic energy. The Cu $2p_{3/2}$ XPS peak meanwhile is at 932.52 eV binding. The summation of the auger kinetic and the XPS binding energies is 1849.22 eV. The intersection of these three numbers on an auger parameters chart confirms that Cu is monovalent.[43]

3.1.2. Average structure. Powder X-ray diffraction (PXRD) of $Mn_{1-x}Cu_{2x}PSe_3$ confirmed solid solution phase purity for $x \leq 0.2$ (Fig. 2(a)) with no additional peaks observed across all compositions. Substitution amounts of $x \geq 0.25$ resulted in Cu_2PSe_3 impurities (Fig. S1). The solid solution, $Mn_{1-x}Cu_{2x}PSe_3$, crystallizes in the same space group as the pure $MnPSe_3$ compound, $R\bar{3}$. Increasing Cu substitution amounts, however, had a major impact on the (00l) and (11l) planes. Increasing x shifts the (006) peak to lower Q values, indicating lattice expansion along the c-axis (Fig. 2(b)). Rietveld refinement of the PXRD data showed that the lattice parameter, c increased from 20.051(1) Å to 20.141(2) Å by increasing x from 0.0 to 0.10. Unlike the peak shift of the (006) peak, the (113) plane showed negligible shift with a major peak broadening, indicating increasing lattice strain along this plane(Fig. 2(c)). Rietveld refinement confirmed that the lattice parameters (Table S1) increased linearly with Cu substitution (Fig. 2(d)). Lattice expansion was found to be highly anisotropic where the c-axis expansion rate with respect to Cu substitution is 10 times that of the a-axis.

3.1.3. Local structure. Fig. 3(a) shows the Pair Distribution Function (PDF) data for all sample compositions. In this analysis, we focused on three interatomic distances, r = 2.24, 2.71, and 3.69 Å, which represent P–Se, Mn–Se, and Mn–Mn interatomic distances in the pure phase of $MnPSe_3$, respectively.

By increasing Cu substitution, we observe peak broadening and an increase in peak intensity in the P–Se peak (r = 2.24 Å) suggesting that Cu(I) is substituted onto a site with a similar interatomic distance (Fig. 3(b)). A noticeable increase in the peak intensity was also observed at r = 3.99 Å, indicating the existence of Cu(I) at this interatomic distance as well (Fig. 3(d)).

Mn–Se and Mn–Mn interatomic distances (r = 2.71 Å and r = 3.69 Å, respectively) were not shifted by Cu substitution (Fig. 3(c) and (d)). Only a decrease in the peak intensity was

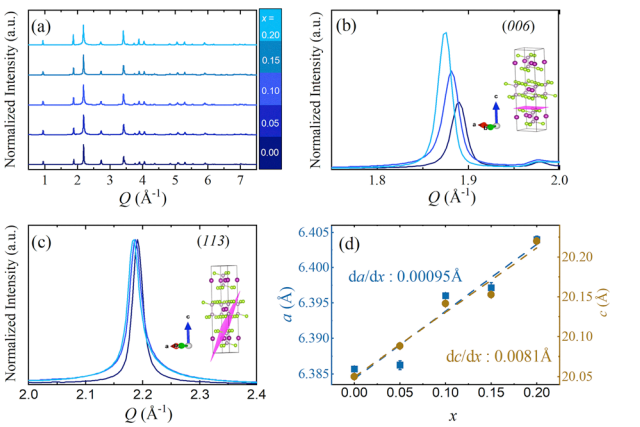

Fig. 2 X-ray diffraction reveals anisotropic lattice expansion with Cu substitution in $MnPSe_3$. (a) PXRD confirms $R\bar{3}$ phase purity of Cu-substituted $MnPSe_3$ powders. (b) With increasing Cu substitution, (006) peaks shift toward lower Q. (c) (113) peaks broaden. The (113) and (006) planes are depicted in the insets. (d) Lattice parameters linearly increase following Vegard's law. The rate of expansion of the c-axis is 10 times that of the a-axis.

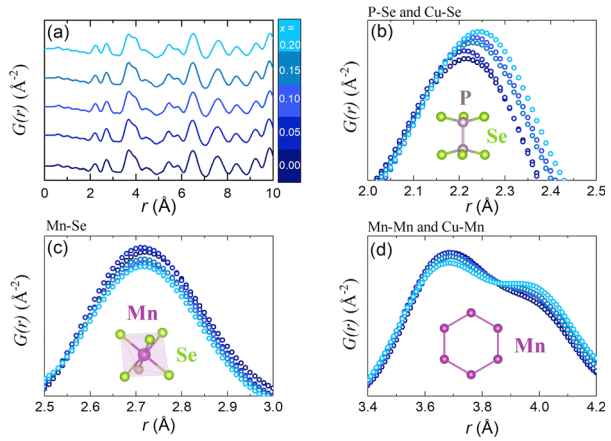

Fig. 3 PDF analysis reveals selective structural changes consistent with Cu incorporation into the $MnPSe_3$ lattice. (a) PDF data of all $Mn_{1-x}Cu_{2x}PSe_3$ samples. (b) P–Se and (c) Mn–Se interatomic spacings. The peak broadness and increase in peak intensity with higher Cu substitution indicate that this interatomic spacing is Cu–Se. The PDF pattern for the Mn–Se peak shows no shift. (d) Mn–Mn interatomic distance remains constant. A noticeable increase in peak intensity at r = 3.99 Å indicates that this interatomic spacing is Mn–Cu. Insets show the interatomic spacings in the structure.

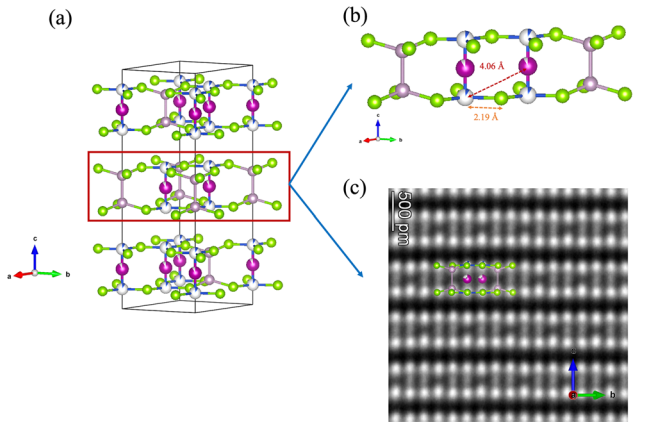

Fig. 4 Atomic model and microscopy confirm Cu site geometry and crystal quality. (a) Crystal lattice of $Mn_{0.9}Cu_{0.2}PSe_3$. (b) Side views of the stacking layer highlight the 2.19 Å Cu–Se and 4.06 Å Cu–Mn interatomic spacings. (c) HAADF-STEM image of a single crystal of $Mn_{0.9}Cu_{0.2}PSe_3$.

observed. The decrease in the peak intensity in these peaks is a result of introducing Mn vacancies with higher substitution levels.

3.1.4. Determining Cu site. PDF analysis located Cu(I) at interatomic spacings of 2.24 Å and 3.99 Å. In addition, XPS confirmed that Cu is monovalent. In order to determine the Cu coordination number, we use the bond valence equation[44]

$$d_{ij} = R_{ij}^{0} - B\ln v_{ij} \quad (1)$$

where d_{ij} is the interatomic spacing for Cu at a value of 2.24 Å. R_{ij}^{0} is an empirical constant specific to cation–anion pair valued at 1.9 for Cu(I) and Se.[45] B is an empirical constant with a value of 0.37.[44] v_{ij} is bond valence which is equivalent to oxidation number/coordination number. The coordination number of 2.51 was calculated using eqn (1), indicating that Cu is trigonally coordinated with Se in the vdW gap.

To achieve this trigonal coordination and maintain the monovalent oxidation state of Cu, we found that Cu(I) is located at (0, 0, 0.083) position above Mn (Fig. 4(a and b)) with bond distances 2.19 Å and 4.06 Å for Cu–Se and Cu–Mn, respectively, in agreement with PDF and XRD analyses. Another possible location for Cu with trigonal coordination is above phosphorous. However, this results in Cu bonded to the divalent $(PSe_3)^{2-}$, contradicting the XPS results. This leaves the Cu atom at the Wyckoff site, 6c in the $R\bar{3}$ space group.[46] However, because of the valency difference between Mn(II) and Cu(I) ions, we are obliged to replace each Mn vacancy with 2 Cu(I) ions not one. Since the $R\bar{3}$ space group doesn't have a Wyckoff site with a 12 multiplicity,[46] we need to introduce another Cu atom with the same interatomic distances and trigonal coordination. Such site is available when we look at a mirror symmetry across the Mn plane, where Mn site is at $\left(0, 0, \frac{1}{6}\right)$. The second Cu site, therefore is at $\left(0, 0, \frac{1}{6} - 0.083 + \frac{1}{6}\right) = (0, 0, 0.25)$.

The final structure shown in Fig. 4(a) maintains the same symmetry elements as the pure $MnPSe_3$ and is similar to the previously studied $Mn_{0.87}Cu_{0.26}PS_3$,[37] where each Mn(II) ion is replaced by two Cu(I) ions above and below it, and Cu(I) ions are in trigonal coordination with Se. Our DFT calculations further confirm our predicted structure, where it shows negative formation energy for substituting Mn with two Cu atoms, while substitution with a single Cu atom showed positive formation energy and thus is energetically unfavorable (Fig. S8). HAADF-STEM image of the crystal shown in Fig. 4(c) confirms the crystallinity and purity of the grown material.

3.2. Magnetic and thermal characterization

FC and ZFC magnetic susceptibility data of $Mn_{1-x}Cu_{2x}PSe_3$ shows that the phases x = 0, 0.05, and 0.1 exhibit antiferromagnetic (AFM) behavior (Fig. 5(a)). The broadness of the AFM transition peak is due to short-range spin correlation.[47] The Néel temperature was, therefore, determined by the maximum point in the dM/dT graph (Fig. S2). The Néel temperature found for $MnPSe_3$ was 68 K, in agreement with previous reports.[1] Néel temperatures for x = 0.05 and 0.1 decreased to 64 K and 58 K respectively. Higher Cu substitution levels (x = 0.15, and 0.2) did not exhibit any magnetic ordering as further confirmed by M *vs.* H hystersis loops (Fig. S3). In addition, no separation between FC and ZFC was observed.

PDF indicates that Mn–Mn on the honeycomb lattice and Mn-Se bonds on the octahedral coordination environment are not affected by Cu substitution. Therefore, the intralayer Mn–Mn magnetic direct exchange interactions (J_1, J_2, and J_3) are not expected to be affected at low substitution levels. Yet, the AFM order is affected by Cu substitution, indicating that other factors play a significant role in the magnetism of $Mn_{1-x}Cu_{2x}PSe_3$.

XRD confirmed that Cu substitution causes lattice expansion along the c-axis, and PDF analysis confirmed that Mn–Se distances remain constant with Cu substitution indicating the layer's width is constant as well. As a result, the vdW gap increases as a function of Cu substitution, affecting the interlayer magnetic exchange

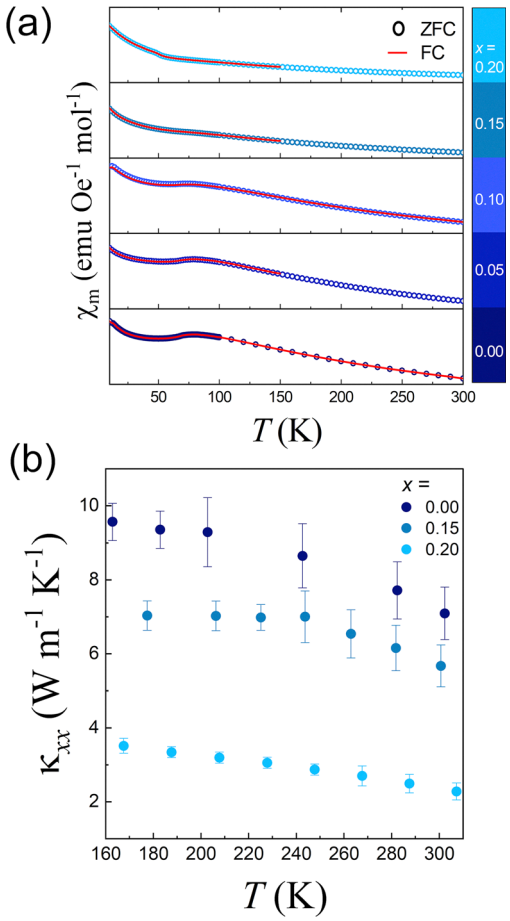

Fig. 5 Magnetic and thermal transport properties evolve with Cu substitution. (a) Magnetic susceptibility measurements show a decrease in the antiferromagnetic ordering temperature with increasing Cu substitutional amounts, x. AFM magnetic ordering is lost at x = 0.15. (b) Thermal conductivity for x = 0, 0.15, and 0.2 decreases with increasing Cu substitution.

interaction (J_c). Even though this exchange parameter is usually small and negligible in vdW materials, neutron studies on $MnPSe_3$ showed that the magnitude of J_c (0.031 meV) is similar to that of J_2 (0.03 meV).[48] Therefore, by varying J_c through increasing the interlayer spacing, a significant impact on the AFM ordering of $MnPSe_3$ is expected. Additionally, by increasing substitution values, more vacancies are introduced onto the Mn site. Magnetic susceptibility confirmed that magnetic order is lost at 15% of Mn vacancies, which is equivalent to one Mn(II) vacancy per honeycomb lattice. The introduction of Mn vacancies is confirmed from ICP and PDF data (Fig. 3(c) and (d)), where the peak intensities decrease by increasing substitution levels. Therefore, establishing a 1:1 correspondence between (x) and the Mn vacancy concentration This would highly affect the intralayer magnetic exchange parameters and contribute to the loss of magnetic ordering.

The effect of introducing Mn vacancies on the magnetic structure is quite similar to substituting non-magnetic ions such as Zn on the honeycomb lattice. This non-magnetic substitution, known also as magnetic dilution, has been previously studied on $MnPS_3$, a sister compound to $MnPSe_3$. It was found that the long-range antiferromagnetic order was maintained up to 50% substitution.[49] However, in our copper substitution, the long-range order was lost at only 15%. This illustrates that magnetic dilution on the honeycomb lattice cannot alone explain this, and that the vdW gap increase must play a significant role. Further neutron diffraction and EXAFS studies could be conducted to further confirm the proposed crystal structure and obtain more robust information about the magnetic structure.

Fig. 5(b) shows the thermal conductivity, κ_{xx} of the solid solution, $Mn_{1-x}Cu_{2x}PSe_3$ for x = 0, 0.15, and 0.2 from 160 K up to 300 K. Thermal conductivity was measured across the *ab* plane on single crystals of the alloys. In the pure phase, $MnPSe_3$, κ_{xx} decreases from 9.5 W mK^{-1} at 160 K to 7 W mK^{-1} at room temperature. This consistent decrease across all samples is due to phonon–phonon scattering that's dominant at high temperatures. By increasing the Cu substitution amounts, κ_{xx} decreases consistently. As x increases, more defects are introduced into the material; this will enhance phonon-defect scattering, and thus lowers the overall thermal conductivity, κ_{xx}.

3.3. Opto-electronic simulation and characterization

3.3.1. Density functional theory. Density functional theory (DFT) calculations were carried out *via* the Vienna *Ab-initio* Simulation Package (VASP) with the inclusion of the projector augmented wave Perdew–Burke–Ernzerhof (PAW-PBE) potentials[50] to simulate the spin resolved electronic band structure of pure $MnPSe_3$ (Fig. 6). Calculations of the band structure for $Mn_{1-x}Cu_{2x}PSe_3$ show minimal changes in the electronic band structure with more Cu substitution (Fig. S7). Furthermore, the magnetic moment of each Mn ion remains almost unchanged confirming that Mn valency remains 2+ with further substitution. The transition dipole moment ($|\vec{D}_{ij}|^2$) between transitions involving initial (i) and final (j) states between bands at high symmetry points are calculated using the equation,

$$\vec{D}_{ij}(\vec{R}_I) = e\left(\int \psi_i^{KS^*}(\vec{R}_I)\vec{r}\psi_j^{KS^*}(\vec{R}_I)d\vec{r}\right) \quad (2)$$

where $\vec{R}_I$ is the position of the ions taken from previous neutron diffraction studies[35] and $\psi_i^{KS^*}(\vec{R}_I)$ and $\psi_j^{KS^*}(\vec{R}_I)$ are the Kohn–Sham wave functions of the initial and final electronic states.[51,52]

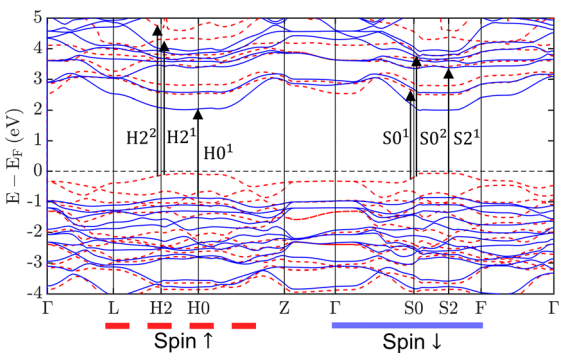

Fig. 6 DFT band structure identifies spin-resolved optical transitions in $MnPSe_3$. DFT calculated spin-resolved band structure of $MnPSe_3$. Highly probable transitions outlined in Table 1 are shown with arrows and labeled.

Table 1 Summary of the predicted most probable transitions occurring at high symmetry points in the Brillouin zone

Label	Transition	$E_j - E_i$ (eV)	$\lvert\vec{D}_{ij}\rvert^2$
$S0^1$	S0-35 → S0-27	2.644	2.798
$H0^1$	H0-25 → H0-26	2.960	0.601
$S2^1$	S2-35 → S2-38	3.535	23.5
$S0^2$	S0-35 → S0-31	3.891	9.457
$H2^1$	H2-35 → H2-41	4.430	6.857
$H2^2$	H2-35 → H2-42	4.803	5.624

The most probable transitions, *i.e.* the transitions with the highest $\vec{D}_{ij}$, are included in Table 1.

3.3.2. Photoluminescence spectroscopy. Due to lack of sample availability, optical measurements could only be carried out on bulk flakes of $MnPSe_3$, $Mn_{0.95}Cu_{0.1}PSe_3$, and $Mn_{0.8}Cu_{0.4}PSe_3$. Low temperature (8 K) and room temperature (300 K) steady state photoluminescence (PL) spectra were obtained for these three samples (Fig. 7(a–c)). A multi-peak fitting routine was employed to fit the PL spectra. Best fits were obtained by fitting for peaks at energies near 2.7 eV and 3.0 eV with Gaussian functions. These fitted peak energies are very close to the predicted energies of the $S0^1$ and $H0^1$ band-to-band transitions. A third higher energy peak centered at approximately 3.55 eV, an energy consistent with the predicted $S2^1$ transition energy, was fit for the data obtained from $MnPSe_3$ and $Mn_{0.8}Cu_{0.4}PSe_3$. It is unclear why this peak was not needed to obtain a close fit to the data obtained from the $Mn_{0.95}Cu_{0.1}PSe_3$ sample. Three sub-band gap exciton peaks were also identified and fit with Lorentzian functions to account for their narrower spectral profile. Nonetheless, the bandwidth of the exciton peaks is large compared to similar studies of excitons in van der Waals materials.[53,54] We attribute this to multiple factors, including the fact that in our study, our measurements were taken on bulk samples as opposed to monolayers and that the spot size of our excitation beam was about 1 mm due to limitations within our setup that necessitated the use of a longer focal length lens "$f = 150$ mm". Additionally, the stronger excitonic absorption in the $Mn_{0.8}Cu_{0.4}PSe_3$ compared to $Mn_{0.95}Cu_{0.1}PSe_3$ and the pristine $MnPSe_3$ is intriguing, but requires further work, *e.g. ab initio* many-body calculations, to understand.

The three exciton peak structure and the spacing of the measured exciton energies are strikingly similarly to exciton energies previously measured in CrI_3 "$E_{ex-A} \approx 1.50$ eV, $E_{ex-B} \approx 1.85$ eV, and $E_{ex-C} \approx 2.20$ eV", a van der Waals magnetic material that has a similar crystal structure to $MnPSe_3$.[55–58] Furthermore, in our measurements, an anomalously large temperature induced red-shift in exciton energy is observed for excitons B and C (X^B and X^C. In the pure $MnPSe_3$ sample, between 8 K and 300 K, the energy of excitons B and C decrease by a magnitude of 35.2 meV and 29.4 meV, respectively (Fig. 7(d)). These energy shifts are significantly higher than that of exciton A, whose energy decreases by merely 7.3 meV with the same increase in temperature.

A reduction in exciton energy with increasing temperature is generally expected across all materials, primarily due to enhanced interactions with phonons at elevated temperatures.

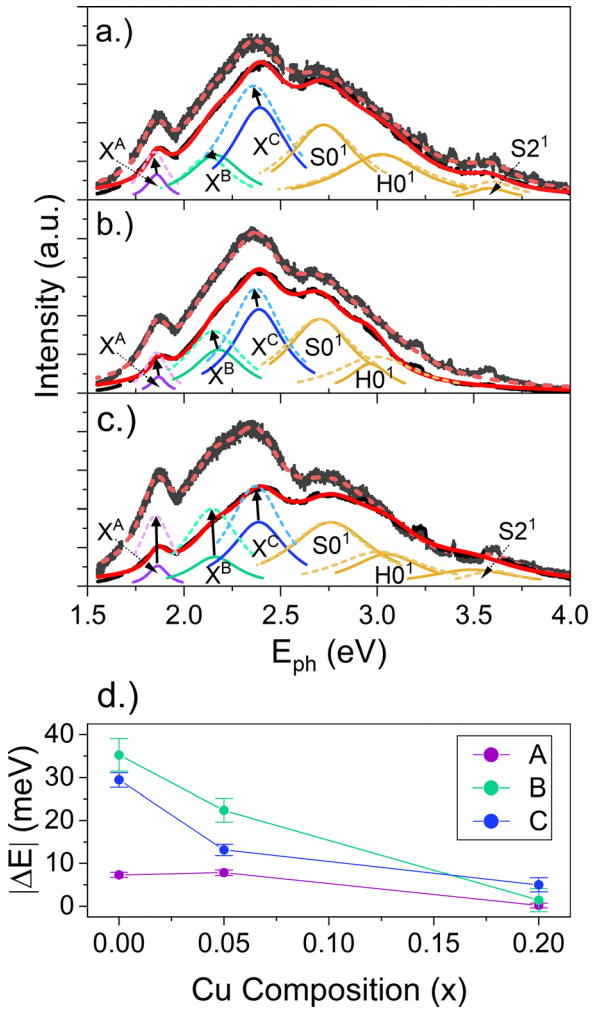

Fig. 7 Photoluminescence spectroscopy reveals temperature-dependent exciton redshift modulated by Cu substitution. Photoluminescence spectra of (a) pure $MnPSe_3$ ($x = 0$), (b) $Mn_{0.95}Cu_{0.1}PSe_3$ ($x = 0.05$), and (c) $Mn_{0.8}Cu_{0.4}PSe_3$ ($x = 0.2$), taken at 8 K (fit plotted with solid line) and 300 K (fit plotted with dashed line). Arrows illustrate redshift in peak position with warming. (d) Magnitude of the temperature-induced redshift of exciton energy for each exciton as a function of Cu composition.

However, in magnetic materials, temperature induced changes in magnetic ordering can also affect exciton energy. Intriguingly, the magnitude of the energy shift for excitons B and C decreases with increasing Cu concentration (Fig. 7(d)). This trend suggests that these excitons' interaction with the magnetic ordering of the material may be responsible for the large temperature induced redshift. Accordingly, the differences in the magnitude of the redshift between the different exciton peaks could be explained by differences in the different excitons' tendency to interact with the ordered Mn(II) $3d^5$ spins that give rise to the AFM order in $MnPSe_3$. Specifically, differences in the orbital character and/or spin state of the excitons would lead to significant differences in how strongly they couple to the magnetic order.[59] The large temperature-dependent redshift of excitons B and C requires extensive further work to explore. Namely, continuous temperature-dependent PL and polarization-resolved, magnetic-field-dependent PL to observe the Zeeman splitting of

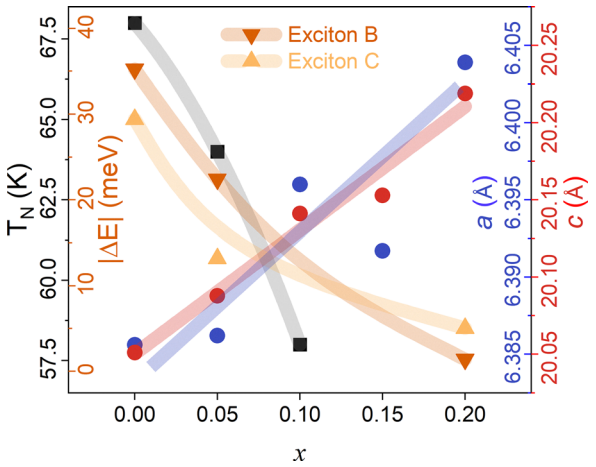

Fig. 8 Summary phase diagram for $Mn_{1-x}Cu_{2x}PSe_3$. Changes in lattice constants *a* and *c*, T_N, and the temperature induced redshift of excitons B and C are plotted as a function of Cu composition, *x*. (Lines are guides to the eye).

exciton states and further probe the coupling of exciton states to the magnetic Mn ions. Such experiments should be the subject of a separate focused study to sufficiently exclude trivial lattice expansion effects and quantitatively correlate the redshift with M(T). Fig. 8 summarizes the structural and functional changes in $MnPSe_3$ with Cu substitution.

3.3.3. Absorption spectroscopy. Room temperature transmission measurements are taken for the $MnPSe_3$, $Mn_{0.95}Cu_{0.1}PSe_3$, and $Mn_{0.8}Cu_{0.4}PSe_3$ single crystals (Fig. 9). Significant interference effects arise in the weak absorption band edge area of the transmission spectra of the $MnPSe_3$ and $Mn_{0.95}Cu_{0.1}PSe_3$ crystals due to interfacial reflections. Interference fringes are fit using an envelope method to obtain approximations of flake thickness "t_{MnPSe_3} = 3.13 μm and $t_{Mn_{0.95}Cu_{0.1}PSe_3}$ = 1.69 μm" and are then removed (supplementary). Interference fringes were not observed in the transmission spectra of the $Mn_{0.8}Cu_{0.4}PSe_3$ flake. Atomic force microscopy was used to measure its thickness "$t_{Mn_{0.8}Cu_{0.4}PSe_3}$ = 0.83 μm". The wavelength dependent absorption coefficient, α is approximated for each of the samples using the formula,

$$\alpha = \frac{\ln\left(\frac{I_0}{I_T}\right)}{t} \quad (3)$$

where I_0 is the intensity of incident light, I_T is the intensity of transmitted light, and *t* is the measured flake thickness. Given that previous studies show the reflectivity of pure $MnPSe_3$ to be in the range $0.18\% < R < 0.28\%$ in the spectral region of interest,[60] failing to account for incident light lost due to reflection should only very marginally affect our calculations of α.

A close fit of the absorption spectra is obtained utilizing Gaussian functions to fit peaks centered at 2.5 eV and 3.0 eV, energies close to the predicted band-to-band transitions $S0^1$ and $H0^1$ (Fig. 9). These energies agree reasonably well with peaks observed in the PL spectra. The energy of the $S0^1$ peak is lower in the absorption measurement due to band tail defect absorption states that lead to the broadening of the absorption

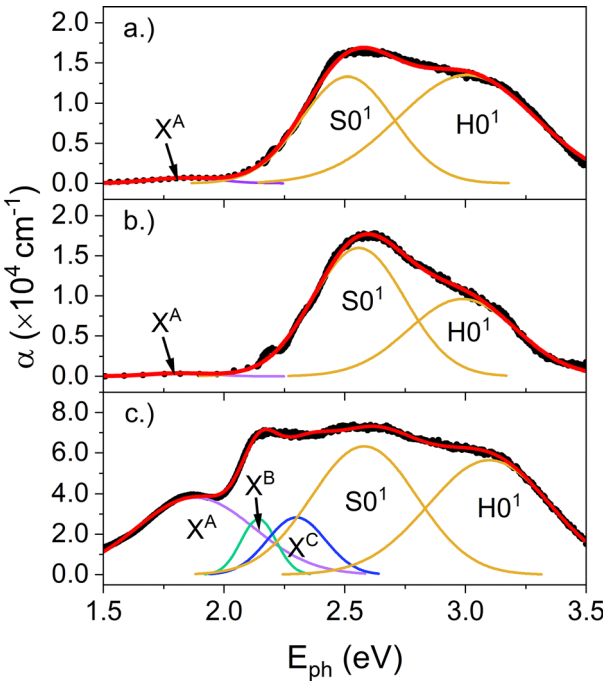

Fig. 9 Optical absorption spectra reveal Cu-dependent evolution of sub-bandgap features. Measured (black) and fitted (red) absorption spectra for (a) pure $MnPSe_3$ (*x* = 0), (b) $Mn_{0.95}Cu_{0.1}PSe_3$ (*x* = 0.05), and (c) $Mn_{0.8}Cu_{0.4}PSe_3$ (*x* = 0.2) single crystals.

band edge. Exciton peaks were fit with Gaussian functions. A peak centered at 1.86 eV, corresponding to the energy at which exciton A was measured in the PL measurements is observed for $MnPSe_3$ and $Mn_{0.95}Cu_{0.1}PSe_3$ samples. Additionally, a close fit to the absorption spectrum of the $Mn_{0.8}Cu_{0.4}PSe_3$ sample could only be acquired by accounting for peaks associated with the B and C excitons. The reason for the lack of absorption related to the B and C excitons in the $MnPSe_3$ and $Mn_{0.95}Cu_{0.1}PSe_3$ samples is unclear. It is possible that the interference effects observed in these two samples hamper our ability to accurately measure absorption associated with those excitons. Lastly, the optical band gap "$E_{g\text{-}opt}$" of the $MnPSe_3$ and $Mn_{0.95}Cu_{0.1}PSe_3$ was approximated using the Tauc method to be 2.295 eV and 2.329 eV, respectively (supplementary). This value of $E_{g\text{-}opt}$ for $MnPSe_3$ lines up with previous experimental reports where the $E_{g\text{-}opt}$ was reported to be 2.27 eV.[60] Unfortunately, the strong exciton absorption in the $Mn_{0.8}Cu_{0.4}PSe_3$ negated the use of the Tauc method. Aligning with the increase of the optical band gap with Cu-composition, the lowest energy SO^1 bulk energy band transition peak is also observed to increase in energy with Cu-composition in both the $MnPSe_3$ and $Mn_{0.95}Cu_{0.1}PSe_3$ samples and continues to increase in the $Mn_{0.8}Cu_{0.4}PSe_3$ sample.

4 Conclusion

We have synthesized and characterized a series of $Mn_{1-x}Cu_{2x}PSe_3$ solid solutions (*x* = 0, 0.05, 0.1, 0.15, and 0.2), demonstrating that Cu substitution introduces systematic structural and functional changes in $MnPSe_3$. X-ray diffraction confirms phase-pure $R\bar{3}$

symmetry across the series. Through our structural analysis, we identified that Cu(I) ions are located in a trigonal coordination with Se.

Magnetic susceptibility measurements reveal a continuous suppression of the Néel temperature with increasing Cu content, culminating in a transition from antiferromagnetic order ($x \leq 0.1$) to a paramagnetic state down to 2 K for $x \geq 0.15$. A modulation of the magnetic exchange parameters is expected due to the observed Cu-substitution-induced lattice expansion, as well as the introduction of Mn vacancies on the honeycomb lattice. A detailed theoretical study is required to elucidate the fundamental mechanism behind these effects.

Photoluminescence spectroscopy identifies three sub-bandgap excitonic features, two of which (B and C) exhibit a redshift with increasing temperature. This redshift is most pronounced in the pristine and $x = 0.05$ samples, where magnetic ordering remains intact, suggesting strong exciton–spin coupling. Absorption spectroscopy further confirms the sub-bandgap features.

Our results demonstrate that non-magnetic Cu substitution in $MnPSe_3$ can be used to tune both structural and magnetic behavior. This work highlights atomic substitution as a robust design strategy to control coupled spin–optical phenomena in layered magnetic semiconductors, opening new opportunities for tailoring 2D materials for spintronic and quantum optoelectronic applications.

Author contributions

R.C.M. and V.D.N. conceived the project; M.N. and S.L. grew and characterized the samples with help from V.D.N.; M.N. conducted magnetic and thermal measurements; A.B. conducted and analyzed photoluminescence and absorption measurements with help from R.C.M.; X.D. conducted DFT calculations with help from W.W.; A.R. conducted HAADF-STEM measurement with help from D.M.; M.N., A.B. and R.C.M. wrote the manuscript with input from all coauthors.

Conflicts of interest

There are no conflicts to declare.

Data availability

Supplementary information (available online) contains additional XRD and magnetometry data, a description of the fitting and analysis of interference fringes in the optical transmission spectra, and details of the electronic structure calculations. Data is available from the corresponding author upon reasonable request.

Supplementary information (SI) is available. See DOI: https://doi.org/10.1039/d6ma00397d.

Acknowledgements

This work was supported by the Center for Emergent Materials, a National Science Foundation (NSF) MRSEC, grant number DMR 2011876. S.L. was supported by OSU start-up funds. We thank Prof. Joseph P. Heremans for inspirational guidance and highly fruitful discussions.

References

1 Z. Ni, A. Haglund, H. Wang, B. Xu, C. Bernhard, D. Mandrus, X. Qian, E. Mele, C. Kane and L. Wu, Imaging the Néel vector switching in the monolayer antiferromagnet MnPSe3 with strain-controlled Ising order, *Nat. Nanotechnol.*, 2021, **16**, 782–787.

2 J.-U. Lee, S. Lee, J. H. Ryoo, S. Kang, T. Y. Kim, P. Kim, C.-H. Park, J.-G. Park and H. Cheong, Ising-Type Magnetic Ordering in Atomically Thin FePS3, *Nano Lett.*, 2016, **16**, 7433–7438.

3 X. Wang, K. Du, Y. Y. Fredrik Liu, P. Hu, J. Zhang, Q. Zhang, M. H. S. Owen, X. Lu, C. K. Gan, P. Sengupta, C. Kloc and Q. Xiong, Raman spectroscopy of atomically thin two-dimensional magnetic iron phosphorus trisulfide (FePS3) crystals, *2D Mater.*, 2016, **3**, 031009.

4 B. Huang, G. Clark, E. Navarro-Moratalla, D. R. Klein, R. Cheng, K. L. Seyler, D. Zhong, E. Schmidgall, M. A. McGuire, D. H. Cobden, W. Yao, D. Xiao, P. Jarillo-Herrero and X. Xu, Layer-dependent ferromagnetism in a van der Waals crystal down to the monolayer limit, *Nature*, 2017, **546**, 270–273.

5 A. Bedoya-Pinto, J.-R. Ji, A. K. Pandeya, P. Gargiani, M. Valvidares, P. Sessi, J. M. Taylor, F. Radu, K. Chang and S. S. P. Parkin, Intrinsic 2D-XY ferromagnetism in a van der Waals monolayer, *Science*, 2021, **374**, 616–620.

6 C. Gong, L. Li, Z. Li, H. Ji, A. Stern, Y. Xia, T. Cao, W. Bao, C. Wang, Y. Wang, Z. Q. Qiu, R. J. Cava, S. G. Louie, J. Xia and X. Zhang, Discovery of intrinsic ferromagnetism in two-dimensional van der Waals crystals, *Nature*, 2017, **546**, 265–269.

7 M. Bonilla, S. Kolekar, Y. Ma, H. C. Diaz, V. Kalappattil, R. Das, T. Eggers, H. R. Gutierrez, M.-H. Phan and M. Batzill, Strong room-temperature ferromagnetism in VSe2 monolayers on van der Waals substrates, *Nat. Nanotechnol.*, 2018, **13**, 289–293.

8 R. Basnet, A. Wegner, K. Pandey, S. Storment and J. Hu, Highly sensitive spin-flop transition in antiferromagnetic van der Waals material MPS3 (M= Ni and Mn), *Phys. Rev. Mater.*, 2021, **5**, 064413.

9 E. C. Ahn, 2D materials for spintronic devices, *npj 2D Mater. Appl.*, 2020, **4**, 1–14.

10 Z. Jia, M. Zhao, Q. Chen, Y. Tian, L. Liu, F. Zhang, D. Zhang, Y. Ji, B. Camargo, K. Ye, R. Sun, Z. Wang and Y. Jiang, Spintronic Devices upon 2D Magnetic Materials and Heterojunctions, *ACS Nano*, 2025, **19**, 9452–9483.

11 M. J. Karaki, X. Yang, A. J. Williams, M. Nawwar, V. Doan-Nguyen, J. E. Goldberger and Y.-M. Lu, An efficient material search for room-temperature topological magnons, *Sci. Adv.*, 2023, **9**, eade7731.

12 M. J. Karaki, A. E. Fahmy, A. J. Williams, S. Haravifard, J. E. Goldberger and Y.-M. Lu, High-throughput search for

topological magnon materials, *arXiv*, 2024, preprint, arXiv:2410.18873, DOI: 10.48550/arXiv.2410.18873.
13 M. Nawwar, R. R. Neumann, J. Wen, A. Mook, I. Mertig and J. P. Heremans, Large Thermal Hall Effect in MnPS3, *Rep. Prog. Phys.*, 2025, **88**, 080503.
14 C. Xu, H. Zhang, C. Carnahan, P. Zhang, D. Xiao and X. Ke, Thermal Hall effect in the van der Waals ferromagnet CrI3, *Phys. Rev. B*, 2024, **109**, 094415.
15 Q. Meng, X. Li, J. Liu, L. Zhao, C. Dong, Z. Zhu, L. Li and K. Behnia, Thermodynamic origin of the phonon Hall effect in a honeycomb antiferromagnet, *arXiv*, 2024, preprint, arXiv:2403.13306, DOI: 10.48550/arXiv.2403.13306.
16 T. T. Mai, K. F. Garrity, A. McCreary, J. Argo, J. R. Simpson, V. Doan-Nguyen, R. V. Aguilar and A. R. H. Walker, Magnonphonon hybridization in 2D antiferromagnet MnPSe3, *Sci. Adv.*, 2021, **7**, eabj3106.
17 J. Luo, S. Li, Z. Ye, R. Xu, H. Yan, J. Zhang, G. Ye, L. Chen, D. Hu and X. Teng, *et al.*, Evidence for topological magnon–phonon hybridization in a 2D antiferromagnet down to the monolayer limit, *Nano Lett.*, 2023, **23**, 2023–2030.
18 J. H. Zhang, L. Lin, S. H. Zheng, P. Z. Chen, L. Huang, G. Z. Zhou, W. J. Zhai, F. Yu, B. Yu, X. M. Cui, M. F. Liu, Y. S. Tang, Z. B. Yan and J.-M. Liu, Weak ferromagnetism and magnetoelectric coupling in van der Waals antiferromagnet MnPSe3, *Appl. Phys. Lett.*, 2024, **124**, 172903.
19 M. Rybak, P. E. Faria Junior, T. Wozniak, P. Scharoch, J. Fabian and M. Birowska, Magneto-optical anisotropies of two-dimensional antiferromagnetic PX_3 from first principles, *Phys. Rev. B*, 2024, **109**, 054426.
20 B. Zheng, J. Fan, B. Chen, X. Qin, J. Wang, F. Wang, R. Deng and X. Liu, Rare-earth doping in nanostructured inorganic materials, *Chem. Rev.*, 2022, **122**, 5519–5603.
21 D. Liang, F. Peng, Q. Du, Y. Zhao and W. Ma, Gadolinium and Europium Doped Chiral Perovskite Films with Magnetic Circular Dichroism and Circularly Polarized Luminescence for Information Encryption Applications, *Angew. Chem., Int. Ed.*, 2025, **64**, e202510754.
22 J. A. Schiemer, R. L. Withers, Y. Liu and M. A. Carpenter, Cadoping of BiFeO3: the role of strain in determining coupling between ferroelectric displacements, magnetic moments, octahedral tilting, and oxygen-vacancy ordering, *Chem. Mater.*, 2013, **25**, 4436–4446.
23 Z. A. VanOrman, M. Cardenes Wuttig, A.-P. M. Reponen, T.-S. Kim, C. E. Casaday, D. Cui, T. Deshpande, H. J. Jobsis, P. Schouwink and E. Oveisi, *et al.*, Metal Doping of Strongly Confined Halide Perovskite Nanocrystals under Ambient Conditions, *J. Am. Chem. Soc.*, 2025, **147**, 16536–16544.
24 F. Wang, T. A. Shifa, P. Yu, P. He, Y. Liu, F. Wang, Z. Wang, X. Zhan, X. Lou and F. Xia, *et al.*, New frontiers on van der Waals layered metal phosphorous trichalcogenides, *Adv. Funct. Mater.*, 2018, **28**, 1802151.
25 M. A. Susner, M. Chyasnavichyus, M. A. McGuire, P. Ganesh and P. Maksymovych, Metal thio-and selenophosphates as multifunctional van der Waals layered materials, *Adv. Mater.*, 2017, **29**, 1602852.
26 D. J. Goossens, A. J. Studer, S. J. Kennedy and T. J. Hicks, The impact of magnetic dilution on magnetic order in MnPS3, *J. Phys.: Condens. Matter*, 2000, **12**, 4233.
27 Y. He, Y.-D. Dai, H. Huang, J. Lin and Y. Hsia, The ordering distribution of the metal ions in the layered cation-mixed phosphorus trisulfides MnxFe1xPS3, *J. Alloys Compd.*, 2003, **359**, 41–45.
28 Y. Takano, A. Arai, Y. Takahashi, K. Takase and K. Sekizawa, Magnetic properties and specific heat of new spin glass Mn0.5Fe0.5PS3, *J. Appl. Phys.*, 2003, **93**, 8197–8199.
29 T. Masubuchi, H. Hoya, T. Watanabe, Y. Takahashi, S. Ban, N. Ohkubo, K. Takase and Y. Takano, Phase diagram, magnetic properties and specific heat of Mn1xFexPS3, *J. Alloys Compd.*, 2008, **460**, 668–674.
30 D. J. Goossens, S. Brazier-Hollins, D. R. James, W. D. Hutchison and J. R. Hester, Magnetic structure and glassiness in Fe0.5Ni0.5PS3, *J. Magn. Magn. Mater.*, 2013, **334**, 82–86.
31 J. N. Graham, M. J. Coak, S. Son, E. Suard, J.-G. Park, L. Clark and A. R. Wildes, Local nuclear and magnetic order in the two-dimensional spin glass Mn0.5Fe0.5PS3, *Phys. Rev. Mater.*, 2020, **4**, 084401.
32 A. Bhutani, J. L. Zuo, R. D. McAuliffe, C. R. dela Cruz and D. P. Shoemaker, Strong anisotropy in the mixed antiferromagnetic system Mn1-xFexPSe3, *Phys. Rev. Mater.*, 2020, **4**, 034411.
33 S. Lee, J. Park, Y. Choi, K. Raju, W.-T. Chen, R. Sankar and K.-Y. Choi, Chemical tuning of magnetic anisotropy and correlations Ni1-xfexPS3, *Phys. Rev. B*, 2021, **104**, 174412.
34 R. Basnet, T. Patel, J. Wang, D. Upreti, S. K. Chhetri, G. Acharya, M. R. U. Nabi, J. Sakon and J. Hu, Understanding and Tuning Magnetism in Layered Ising-Type Antiferromagnet FePSe3 for Potential 2D Magnet, *Adv. Electron. Mater.*, 2024, **10**, 2300738.
35 A. Wiedenmann, J. Rossat-Mignod, A. Louisy, R. Brec and J. Rouxel, Neutron diffraction study of the layered compounds MnPSe3 and FePSe3, *Solid State Commun.*, 1981, **40**, 1067–1072.
36 Y. Mathey, R. Clement, J. P. Audiere, O. Poizat and C. Sourisseau, Structural, vibrational and conduction properties of a new class of layer-type MPS3 compounds: MnII1x-MI2xPS3 (MI = Cu, Ag), *Solid State Ionics*, 1983, **9–10**, 459–465.
37 Y. Mathey, A. Michalowicz, P. Toffoli and G. Vlaic, Resolution of a structural disorder through apparently inconsistent x-ray diffraction and EXAFS data: structure of the new layered system manganese copper phosphorus sulfide (Mn1-xCu2x)PS3 (x = 0.13), *Inorg. Chem.*, 1984, **23**, 897–902.
38 A. Kuhn, L. M. Schoop, R. Eger, I. Moudrakovski, S. Schwarzmüller, V. Duppel, R. K. Kremer, O. Oeckler and B. V. Lotsch, Copper Selenidophosphates Cu4P2Se6, Cu4P3Se4, Cu4P4Se3, and CuP2Se, Featuring Zero-, One-, and Two-Dimensional Anions, *Inorg. Chem.*, 2016, **55**, 8031–8040.
39 P. Juhás, T. Davis, C. L. Farrow and S. J. Billinge, PDFgetX3:a rapid and highly automatable program for processing powder diffraction data into total scattering pair distribution functions, *Appl. Crystallogr.*, 2013, **46**, 560–566.

40 B. H. Toby and R. B. Von Dreele, GSAS-II: the genesis of a modern open-source all purpose crystallography software package, *Appl. Crystallogr.*, 2013, **46**, 544–549.
41 N. Fairley, V. Fernandez, M. Richard-Plouet, C. Guillot-Deudon, J. Walton, E. Smith, D. Flahaut, M. Greiner, M. Biesinger and S. Tougaard, *et al.*, Systematic and collaborative approach to problem solving using X-ray photoelectron spectroscopy, *Appl. Surf. Sci. Adv.*, 2021, **5**, 100112.
42 T. Fleisch and G. Mains, Reduction of copper oxides by UV radiation and atomic hydrogen studied by XPS, *Appl. Surf. Sci.*, 1982, **10**, 51–62.
43 J. Chastain and R. C. King Jr, Handbook of X-ray photoelectron spectroscopy, PerkinElmer Corporation, 1992, **40**, 25.
44 P. M. Woodward, P. Karen, J. S. Evans and T. Vogt, *Solid state materials chemistry*, Cambridge University Press, 2021.
45 I. D. Brown, *The chemical bond in inorganic chemistry: the bond valence model*, Oxford university press, 2016, vol. 27.
46 C. P. Brock, T. Hahn, H. Wondratschek, U. Müller, U. Shmueli, E. Prince, A. Authier, V. Kopsky, D. Litvin, E. Arnold *et al.*, International tables for crystallography volume A: Space-group symmetry, Wiley Online Library, 2016.
47 P. Jeevanandam and S. Vasudevan, Magnetism in MnPSe3:a layered 3d5 antiferromagnet with unusually large XY anisotropy, *J. Phys.: Condens. Matter*, 1999, **11**, 3563.
48 S. Calder, A. V. Haglund, A. I. Kolesnikov and D. Mandrus, Magnetic exchange interactions in the van der Waals layered antiferromagnet Mn P Se 3, *Phys. Rev. B*, 2021, **103**, 024414.
49 D. J. Goossens and T. J. Hicks, The magnetic phase diagram of, *J. Phys.:Condens. Matter*, 1998, **10**, 7643.
50 P. E. Blöchl, Projector augmented-wave method, *Phys. Rev. B:Condens. Matter Mater. Phys.*, 1994, **50**, 17953–17979.
51 L. Kronik, T. Stein, S. Refaely-Abramson and R. Baer, Excitation Gaps of Finite-Sized Systems from Optimally Tuned Range-Separated Hybrid Functionals, *J. Chem. Theory Comput.*, 2012, **8**, 1515–1531.
52 D. J. Vogel and D. S. Kilin, First-Principles Treatment of Photoluminescence in Semiconductors, *J. Phys. Chem. C*, 2015, **119**, 27954–27964.
53 M. M. Ugeda, A. J. Bradley, S.-F. Shi, F. H. da Jornada, Y. Zhang, D. Y. Qiu, W. Ruan, S.-K. Mo, Z. Hussain, Z.-X. Shen, F. Wang, S. G. Louie and M. F. Crommie, Giant bandgap renormalization and excitonic effects in a monolayer transition metal dichalcogenide semiconductor, *Nat. Mater.*, 2014, **13**, 1091–1095.
54 J. Huang, T. B. Hoang and M. H. Mikkelsen, Probing the origin of excitonic states in monolayer WSe2, *Sci. Rep.*, 2016, **6**, 22414.
55 I. Pollini and G. Spinolo, Intrinsic Optical Properties of CrCl3, *Phys. Status Solidi B*, 1970, **41**, 691–701.
56 V. M. Bermudez and D. S. McClure, Spectroscopic studies of the two-dimensional magnetic insulators chromium trichloride and chromium tribromide—I, *J. Phys. Chem. Solids*, 1979, **40**, 129–147.
57 K. L. Seyler, D. Zhong, D. R. Klein, S. Gao, X. Zhang, B. Huang, E. Navarro-Moratalla, L. Yang, D. H. Cobden, M. A. McGuire, W. Yao, D. Xiao, P. Jarillo-Herrero and X. Xu, Ligand-field helical luminescence in a 2D ferromagnetic insulator, *Nat. Phys.*, 2018, **14**, 277–281.
58 W. Jin, H. H. Kim, Z. Ye, G. Ye, L. Rojas, X. Luo, B. Yang, F. Yin, J. S. A. Horng, S. Tian, Y. Fu, G. Xu, H. Deng, H. Lei, A. W. Tsen, K. Sun, R. He and L. Zhao, Observation of the polaronic character of excitons in a two-dimensional semiconducting magnet CrI3, *Nat. Commun.*, 2020, **11**, 4780.
59 N. J. Brennan, C. A. Noble, J. Tang, M. E. Ziebel and Y. J. Bae, Important Elements of Spin-Exciton and Magnon-Exciton Coupling, *ACS Phys. Chem. Au*, 2024, **4**, 322–327.
60 V. Grasso and L. Silipigni, Optical absorption and reflectivity study of the layered MnPSe3 seleniophosphate, *J. Opt. Soc. Am. B*, 1999, **16**, 132–136.